AIP | Review of Scientific Instruments

# A novel optical apparatus for the study of rolling contact wear/fatigue based on a high-speed camera and multiple-source laser illumination

I. Bodini, G. Sansoni, M. Lancini, S. Pasinetti, and F. Docchio

Citation: Review of Scientific Instruments **87**, 083701 (2016); doi: 10.1063/1.4959981
View online: http://dx.doi.org/10.1063/1.4959981
View Table of Contents: http://scitation.aip.org/content/aip/journal/rsi/87/8?ver=pdfcov
Published by the AIP Publishing



# A novel optical apparatus for the study of rolling contact wear/fatigue based on a high-speed camera and multiple-source laser illumination

I. Bodini,[1,a)] G. Sansoni,[2] M. Lancini,[1] S. Pasinetti,[2] and F. Docchio[1]
[1]*Department of Mechanical and Industrial Engineering, University of Brescia, Brescia 25123, Italy*
[2]*Department of Information Engineering, University of Brescia, Brescia 25123, Italy*

(Received 15 April 2016; accepted 17 July 2016; published online 2 August 2016)

Rolling contact wear/fatigue tests on wheel/rail specimens are important to produce wheels and rails of new materials for improved lifetime and performance, which are able to operate in harsh environments and at high rolling speeds. This paper presents a novel non-invasive, all-optical system, based on a high-speed video camera and multiple laser illumination sources, which is able to continuously monitor the dynamics of the specimens used to test wheel and rail materials, in a laboratory test bench. 3D macro-topography and angular position of the specimen are simultaneously performed, together with the acquisition of surface micro-topography, at speeds up to 500 rpm, making use of a fast camera and image processing algorithms. Synthetic indexes for surface micro-topography classification are defined, the 3D macro-topography is measured with a standard uncertainty down to 0.019 mm, and the angular position is measured on a purposely developed analog encoder with a standard uncertainty of 2.9°. The very small camera exposure time enables to obtain blur-free images with excellent definition. The system will be described with the aid of end-cycle specimens, as well as of in-test specimens. *Published by AIP Publishing.* [http://dx.doi.org/10.1063/1.4959981]

## I. INTRODUCTION

Monitoring wear and rolling contact fatigue (RCF) between wheels and rails is mandatory to increase safety in train transportation.[1,2] On-site inspection methods, originally based almost exclusively on visual inspection, have been developed over the years. They use various non-destructive inspection techniques such as eddy current testing,[3] electromagnetic tomography,[4] axle box acceleration measurements,[5] vision systems, and/or laser stripes mounted on trains to detect rail conditions.[6–8] Laboratory methods are routinely used: they include full-scale Laboratory experiments,[9] scale-down tests,[10] and bench tests by twin-disc machines.[11–14]

In twin-disk tests, disk-shaped rail-wheel couples, with controlled contact load, rotate at variable speed, for predefined time intervals. It is therefore possible to perform accelerated wear and RCF tests with nominal contact pressures varying over wide ranges, using different materials, and in different operating conditions. Following the time evolution of the surface topology requires that the tests are interrupted at different times and that destructive analysis is carried out. In most cases, optical methods are used to perform this task, such as white light confocal microscopy[11] and scanning electron microscope (SEM) image analysis.[13,14] Image acquisition of the specimens at a macro-scale is also carried out to record the surface evolution during the tests, and to correlate it to the information from the micro-scale.[15]

In a companion laboratory of our department, a detailed analysis of RCF and wear on wheel-rail pairs is underway, in the framework of an industrial research aimed at improving the wheel and rail performance and lifetime. Dry and wet tests are conducted on a twin-disk machine to reproduce the different environmental conditions for train transportation. Microscope analysis is performed at the test end. Subsequent versions of the testing apparatus have been presented,[16–18] where vibrations and torque of the test bench are monitored, to provide a powerful means to early detect RCF cracks and continuous wear observation.

To further improve the RCF and wear apparatus, a novel design of a camera system, and of the respective illumination geometry, was required for on-line, real-time acquisition of the specimens, which rotate at a speed of 500 rpm (≈8.3 Hz), and for quantitative analysis of the surface topography evolution during the tests. This vision-based system should avoid image blurring even at the highest specimen rotation speeds: high acquisition frequencies and low frame exposure times are required, without decreasing image resolution, brightness, and specimen speed. This is possible using the new generation of high-speed video cameras, which are able to acquire images at very high frame-rates, as demonstrated in Ref. 19 in the case of fatigue tests in polymeric materials.

The use of high speed cameras for quantitative process analysis requires a good visibility of the image features. Therefore, the spatial resolution had to be carefully chosen, and a proper illumination had to be considered. 2D imaging could then be combined with 3D imaging obtained by optical triangulation,[20–23] by adding structured light sources. An additional requirement was the non-contact measurement of the angular position of the disk, since this information was not available in the test bench. In addition, the tests are usually time consuming, and this results in large hard disk occupation and long frame elaboration time. Thus image analysis should be fast and provide good performance. Finally, to reach a good compromise between the significance of the monitoring and memory occupation, triggered acquisition was desirable: the trigger

a)Electronic mail: ileana.bodini@unibs.it

should be automatically activated by a single event, such as a vibration signal induced by the specimen deterioration,[16] or a periodical signal, conveniently set to guarantee a complete monitoring of the test.

The effectiveness of camera imaging and analysis in damage monitoring is well documented in the literature. For example, in Refs. 24–27, the statistical properties of binary speckle images are used to measure the surface roughness: suitable thresholding is applied to the image, and dark and bright regions are detected using microscope optics, on a 2 $mm^2$ area. They are counted and analyzed to establish a correlation between the measured quantities and the roughness parameters. In Ref. 27, Gabor filters are proposed for the detection of the image micro-texture, which is related to the particular wear phenomenon under inspection, characterized by repetitive patterns (corrugations).

We focused on the dimensioning of the optical system, on the choice of the optimal illumination solutions for 2D and 3D specimen monitoring, on the design of an angular encoder, on its independent illumination source, and on the development of the proper image analysis procedures. In this paper, we describe the development of the laboratory prototype of the optical apparatus, from both the hardware and software viewpoints. We also report the on-site characterization and calibration, and the initial results of the tests on rolling contact specimens.

## II. SYSTEM REQUIREMENTS

The purposes of the vision-based measurement system integrated with the RCF test bench are (i) continuous 2D/3D monitoring of the specimen surface and (ii) angular position measurement of the specimen, to synchronize the specimen surface image with the angular position. The former objective is relevant in the improvement of the models that predict the interactions between wear and fatigue.[16–18] As to the angular measurements, they allow to follow the evolution of a single portion of specimen surface, and to determine the position of an occurred event and to correlate this event with other model parameters, such as vibration level and torque, to more accurately calculate the coefficient of friction.[16–18] The independent, optical approach in the angular measurement would not have been necessary, had the angular information from the rotation axis been available in the RCF apparatus. Its absence forced us to develop this solution.

The main requirements of the optical system, as agreed with the experts from the companion laboratory, were as follows:

- 2D measurements with dimensions of the order of 0.01 mm;
- 3D measurements with dimension of the order of 0.1 mm;[17]
- angular position measurements with standard uncertainties of 5° (these are, in any case, lower than those obtained indirectly from torque measurements).[17]

The constraints in the optical system design were as follows:

- a rotational frequency of the specimen of about 8.3 Hz;
- an available input window of 120 mm × 70 mm to position the optical axis of the camera perpendicularly to the rotation axis of the specimen, combined to another window of 120 mm × 100 mm that forms a 135°-angle with respect to the former one, and permits the triangulation[20–23] with a laser stripe (Section III);
- a minimum distance between the specimen and the entrance pupil of the camera lens of 240 mm.

## III. THE OPTICAL APPARATUS

### A. Optical geometry

Fig. 1 shows the geometry of the optical system and the parameters involved in the design process. Image plane κ represents the video camera, f is its optical focal length, and point C is its entrance pupil. Parameters c and r index the image columns and rows. The camera reference system is $\{X_C, Y_C, Z_C\}$, centered at point C, with $X_C$ parallel to the rotation axis R. Axis $Z_C$ is the camera optical axis, intersecting plane κ at point O′ $(c_0, r_0)$. The specimen S, with diameter D and height H, rotates around axis R. $Z_c$ intersects S at point O, which is the origin of the global reference system {X, Y, Z} oriented as in the figure. P is a generic point on the specimen surface. L = $\overline{OC}$ is the stand-off distance. FOVx and FOVy are the dimensions of the Field-of-View along X and Y, respectively.

The main parameter for the design of the vision system is the camera acquisition speed $f_c$ (frames per second, fps), related to the peripheral rotation speed of a point P on the disk $v_p$ and to the frame height by

$$f_c = \frac{v_P}{FOVy}. \quad (1)$$

At the maximum rotation speed of 500 rpm (8.3 Hz), for D = 60 mm and H = 15 mm, the velocity $v_P$ is $v_P = 60\ mm \times \pi \times 8.3/s = 1570\ mm/s$. A trade-off between FOVy and $f_c$ must be chosen: in fact, high $f_c$ values can be obtained with small values of FOVy (i.e., a small camera resolution), whereas a high FOVy yields a low value of the spatial resolution Ry, and

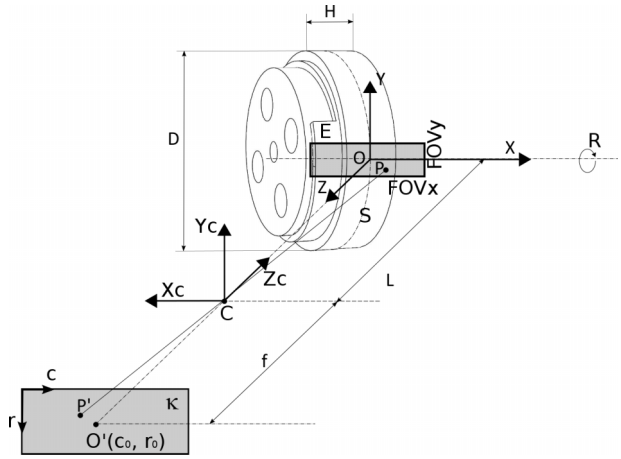


FIG. 1. Geometry of the optical system and parameters involved in the design process. S: specimen, E: encoder, C: high-speed camera.

a low image visibility. With the geometry of Fig. 1, varying FOVy between 3 mm and 10 mm results in $f_c$ varying between 523 fps and 157 fps. As a trade-off, a value of FoVy = 6.5 mm, corresponding to a value of $f_c$ equal to at least 262 fps, was necessary. Among the available cameras on the market, with a wide range of resolutions, communication protocols, technology, speed, and cost, the PROMON 501–AOS by Technologies AG was our solution. The camera can operate from 85 fps to 3391 fps, at correspondingly decreasing values of the camera resolution. Exposure times are software-adjustable from 13 $\mu$s to $1/f_c$.[28]

For this camera, the combination $f_c = 377$ fps, $R_r = 240$ px, and $R_c = 1280$ px was then selected. Correspondingly, a spatial resolution $R_y = 0.027$ mm/px was obtained, suitable for a reliable acquisition of features up to 0.011 mm.[29] The optical magnification M is

$$M = \frac{Ry \times P_{Size}}{FOVy} = 0.203, \quad (2)$$

where $P_{Size} = 5.5$ $\mu$m is the camera pixel size. The camera focal length f was chosen by setting L = 240 mm as the distance of the disk under test in the test bench, and by using the Gaussian form of the thin lens equation

$$\frac{1}{L} + \frac{1}{s_i} = \frac{1}{f}, \quad (3)$$

where $s_i = M \times L$ is the lens-image plane distance. From Eq. (3), f has been calculated, obtaining f = 52.3 mm, which could be replaced by the available f = 50 mm camera lens. With this lens, the field of view is FoVx = 35 mm, and the corresponding spatial resolution was $R_x = 0.027$ mm/px.

### B. The linear encoder for the angular position measurement

To measure the angular position of the rotating specimen, a purposely designed encoder E, schematically shown in Fig. 1 was worked on a CNC (Computer Numerical Control) machine. This component has a diameter $D_E = 50$ mm and a linearly varying profile height along the circumference from 3 to 8 mm. The encoder was coaxially mounted on the specimen (see Fig. 1, identified by E) so that both could be imaged at plane κ. Thus, the measurement of the encoder profile height in each image allows to measure the angular position of the specimen.

### C. Illumination sources and regions of interest (ROIs)

The choice of the illumination sources was made to accomplish three requirements. The first was the wide-area illumination of the sample surface to allow 2D imaging of the surface in front of the camera. The second was the sidewise line-shaped illumination of a section of the surface to measure its depth through optical triangulation. The third was the line-shaped illumination of the encoder to measure the specimen's angular position. In all cases, low-blurring and low-noise monitoring of the rotating specimens and of the encoder required camera exposure times in the microsecond range: the specimen illumination was a critical issue to obtain

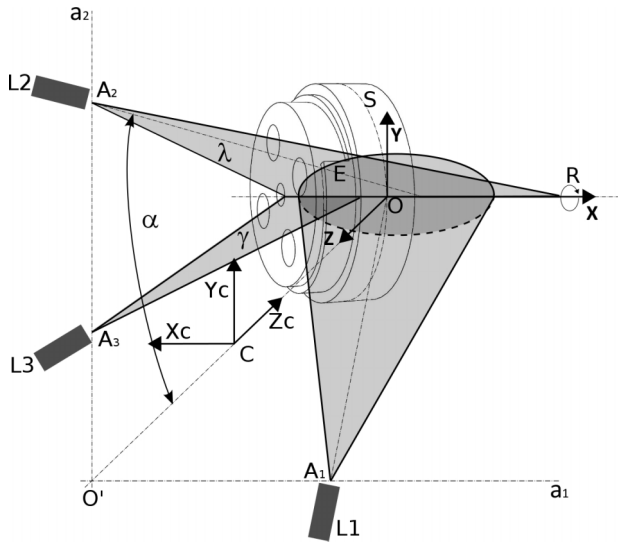


FIG. 2. Geometry of the illumination of the optical system. L1: diffusely diverging laser, L2: laser stripe for 3D measurements, and L3: laser stripe for the measurement of the angular position.

images with clear features at such a short exposures. Both incoherent and coherent sources were considered: eventually, laser sources were chosen as the sources providing the best levels of feature visibility and a low signal-to-noise ratio. Semiconductor laser modules (Lasiris™ SNF Laser), emitting 10 mW at 670 nm, were used. Their emission is polarized and can be intensity-adjusted by means of a second polarizing filter. The two of them (L1, diffusely diverging, and L2, line-shaped) were used to illuminate the specimen, and the third one (L3, line-shaped) to illuminate the encoder.

The geometry of illumination is shown in Fig. 2. L1 is positioned at point $A_1$, along line $a_1$, parallel to X and intersecting O′. The beam, directed towards point O, is properly defocused to diffusively illuminate the specimen. L2 is positioned at point $A_2$, along line $a_2$, parallel to Y and intersecting O′. The beam is line-shaped and propagates as a light plane, λ in the figure, at an angle α with respect to plane XZ. The intersection of plane λ with the specimen surface results as a line profile LP2, passing through point O and parallel to X. Finally, laser L3 is positioned at point $A_3$: like L2, it projects a light plane, γ in the figure, which intersects the specimen surface along X. A narrow aperture of L3 limits the illumination to the encoder surface alone.

Fig. 3 shows the specimen S and the encoder E illuminated by the three sources: in particular, Fig. 3(a) shows the illumination by the diffused source L1: the diffused light pattern (LD) shows bright and dark regions due to the effects of speckle. Fig. 3(b) shows the illumination by the line-shaped source L2 along the plane λ: the deformation induced on the laser profile LP2 by the specimen surface is visible. Fig. 3(c) shows the laser profile LP3 on the encoder.

In the images acquired by the camera, three Regions of Interest (ROIs) were selected to isolate the most significant portions for the elaboration of each image. Each elaboration procedure operates on a specific ROI: in Figs. 3(d)–3(f) the ROI1, ROI2, and ROI3 corresponding to the three above illumination sources are illustrated (grey levels are inverted to

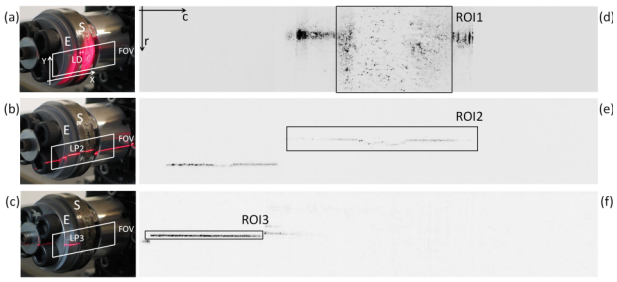


FIG. 3. Specimen (S) and encoder (E) in three different illumination conditions and the respective Regions of Interests (ROIs). The field of view (FOV) is also shown. (a) and (d): Diffused LD pattern on S and ROI1; (b) and (e): LP2 laser pattern on S and ROI2; (c) and (f): LP3 laser profile on E and ROI3. Grey levels of the images have been inverted to enhance the visibility of both the blobs and the laser stripes.

highlight the details). ROI1 and ROI2 overlap in space, but not in time, as it will be shown in Section V.

### D. Working layout of the optical apparatus

The layout of the optical apparatus is shown in Fig. 4. Laser projectors L1, L2, and L3 and the camera are assembled following the geometry explained in Section III.

The apparatus uses, for image acquisition and analysis, a PC (ASUSTeK Computer, Inc., Processor Intel® Core™ i7-3770 CPU at 3.40 GHz, RAM 8.00 GB), equipped with a dedicated hard disk (SSD 240 GB, Kingston V300 HD) for data storing. A proprietary software (AOS PROMON Studio) allows to select the camera parameters (resolution, gain, exposure time, pre-triggered interval, and acquisition mode). Data storage is carried out by the embedded saving functions of the software, which assemble the frame sequences into suitable video files.

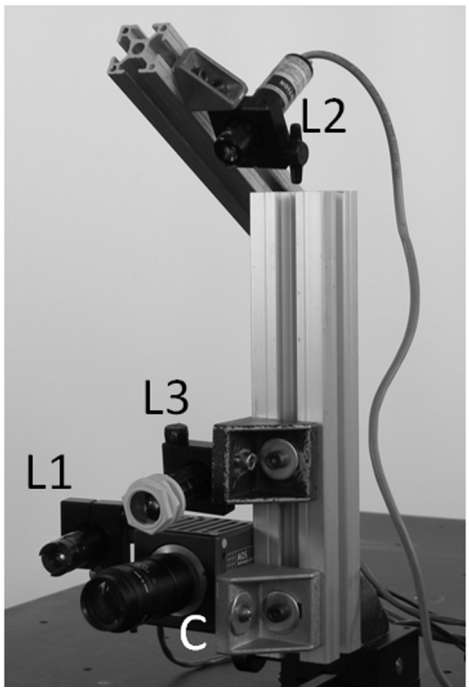


FIG. 4. Experimental setup of the optical apparatus.

## IV. IMAGE ANALYSIS PROCEDURES

### A. Diffuse light image analysis on ROI1

The scattered light pattern shown in Fig. 3(d) exhibits bright areas having number, dimension, position, shape, and orientation that can be correlated to the formation of small dips and crests during wear and RCF processes. To analyze such non-texturized discrete defects, blob analysis was considered to be ideal. Firstly, image thresholding was used to highlight bright areas with respect to the background, and to detect a blob in correspondence with each pixel group within a closed line in the image foreground.[30] The blob analysis allows us to derive a number of parameters, such as the number of blobs, their area, their orientation, and their linear dimensions, which are the height and width of the rectangles that circumscribe the blobs. The blobs are subdivided in classes $C_i$ according to their area. For each i-th class, the following parameters are computed: (i) the number $n_{B,i}$ of the blobs in ROI1, (ii) the area $a_{B,i}$, i.e., the average area of the blobs of the i-th class, (iii) the damage ratio $r_{Bi}$, i.e., the total area occupied by the blobs of the i-th class, with respect to the overall area of ROI1, and (iv) the asymmetry index $As_{B,i}$, i.e., the height/width ratio of the rectangles that circumscribe the blobs. In addition, the average of parameters $n_B$, $a_{B,i}$, and $r_{B,i}$, over all the classes, has been calculated. Each average value has been defined as (v) $N_B$, (vi) $A_B$, and (vii) $R_B$, respectively.

Parameter $r_{B,i}$ is

$$r_{B,i} = \frac{A_{B,i}}{A_{ROI1}}, \tag{4}$$

where $A_{B,i}$ is the sum of the areas of the blobs belonging to class Ci, and $A_{ROI1}$ is the total area of ROI1.

Parameter $As_{B,i}$ is

$$As_{B,i} = \frac{H_{B,i}}{W_{B,i}}, \tag{5}$$

where $H_{B,i}$ and $W_{B,i}$ are the average height and width of the bounding rectangles for each blob of a certain class of area $C_i$. To monitor the temporal evolution of a specimen during a rolling contact fatigue test, videos of suitable length are acquired; the above parameters have been calculated on all the frames of each video.

### B. Light plane image analysis on ROI2

The aim of the procedure applied to ROI2 is to measure the spatial coordinates of the surface points belonging to laser line LP2 in the global reference system {X, Y, Z}. Optical triangulation is used to perform this task.[20–23] The method is based on the observation that, given a point P on line LP2, it can be viewed as the intersection between plane λ and the line of sight PP′. As shown in Ref. 31, the position of point P can be calculated by solving a linear system of three equations where the unknowns are the coordinates $\{X_P, Y_P, Z_P\}$. The coefficients of the first two equations are obtained by estimating (i) the roto-translation parameters of the camera system $\{X_C, Y_C, Z_C\}$ with respect to {X, Y, Z}, (ii) the focal length f, and (iii) the position $(c_0, r_0)$ of point O′ (camera calibration). The coefficients of the third equation are obtained

by estimating the orientation of plane λ in the global reference {X, Y, Z} (laser plane calibration). The known terms of the system equations are represented by the image coordinates ($c_P$, $r_P$) of point P′.

### 1. Camera calibration

To estimate the camera parameters,[31] the well-known pinhole camera model has been chosen. These are the nine $\{r_{ij}\}$ elements of the rotation matrix between the camera system and the global system, the three elements $[t_x, t_y, t_z]$ of the translation vector $\overline{OO'}$, the focal length f, the scale factors $s_c$, $s_r$ along the image columns and rows, and the coordinates $c_0$, $r_0$ of point O′. Considering point P and its conjugate P′ at the image plane, the line of sight $\overline{PP'}$ can be expressed as follows:

$$\begin{cases} c_p = s_c \cdot f \cdot \dfrac{r_{11}X_p + r_{12}Y_p + r_{13}Z_p + t_x}{r_{11}X_p + r_{12}Y_p + r_{13}Z_p + t_z} + c_0 \\ r_p = s_r \cdot f \cdot \dfrac{r_{11}X_p + r_{12}Y_p + r_{13}Z_p + t_y}{r_{11}X_p + r_{12}Y_p + r_{13}Z_p + t_z} + r_0 \end{cases}. \quad (6)$$

Since we have two equations and eleven unknowns, at least six points in the global reference must be used. These points are defined using the master shown in Fig. 5(a). This master, 65 mm in height and 80 mm in width, has the form of a matrix of black circles on a white background. It has a controlled planarity (in the order of 100 $\mu$m) and is rigidly mounted on a translation stage with positioning resolution of 0.01 mm, oriented along axis Z. Circle rows and columns are oriented along X and Y, respectively: each circle has a diameter of 0.4 mm, their inter-centre distance being 1.2 mm.

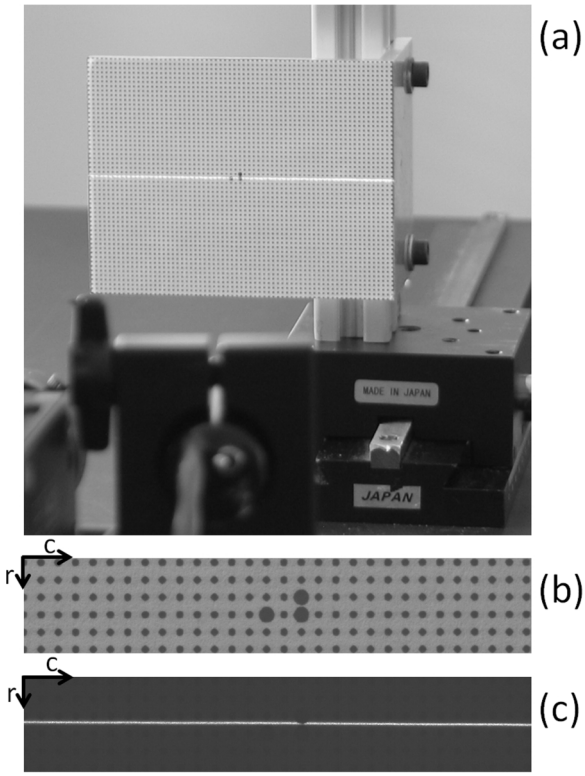


FIG. 5. 3D camera-laser calibration. (a) Calibration master. (b) Acquired image of the master. (c) Acquired image of the laser profile LP2 at the range-center. The line is oriented parallel to X (Xc and c) and is positioned in the middle of the image.

A dedicated procedure acquires the image of the master (Fig. 5(b)), thresholds it, corrects for distortions and perspective,[32,33] and calculates the coordinates $c_M$, $r_M$ of the centroid M of each circle. A suitable number of circles are chosen to feed the pin-hole model (calibration markers); for each one, both the image coordinates ($c_M$, $r_M$) and the global coordinates ($X_M$, $Y_M$, $Z_M$) of the centroid are used in Eq. (6). This procedure is repeated at different positions $Z_n$ of the master along coordinate Z: Fig. 5(c) shows the laser profile LP2 corresponding to the master position at half Z range. The objective focal distance is adjusted so that in this position the camera acquires at optimal focus.

The method used to solve the over-determined resulting system is well known: the reader can refer to Ref. 31 for further details. Here, it is worth noting that the problem is linear, and a maximum likelihood criterion is used to estimate the unknowns.

### 2. Laser plane calibration

This procedure is aimed at estimating the orientation of plane λ with respect to the reference system {X, Y, Z}. The plane is modeled as

$$Z_\lambda = AX_\lambda + BY_\lambda + C, \quad (7)$$

where ($X_\lambda$, $Y_\lambda$, $Z_\lambda$) are the coordinates of the points belonging to the plane. To estimate coefficients A, B, and C, for each known position $Z_n$ of the master, the corresponding laser profile is acquired, obtaining a set of line profile parallel to that of Fig. 5(c), but shifted upwards or downwards. Prior to the calibration of the plane, centers of gravity ($c_G$, $r_G$) of the line profile were calculated, where $c_G$ is the column index of the image, and $r_G$ is the weighted average of the grey levels $l_r$ of the image pixels belonging to that column, i.e.,

$$r_G = \frac{\sum_r l_r \cdot r}{\sum_r r}. \quad (8)$$

The vector $G_n$ with elements $\{c_G, r_G\}_n$ and the corresponding values $Z_n$ are inserted in Eq. (6): since the camera parameters are known, it is possible to calculate the unknowns $X_\lambda$ and $Y_\lambda$. A cloud of points representing plane λ is obtained. Their coordinates are used to fit coefficients A, B, C in Eq. (7). Since the problem is linear, a simple linear regression algorithm is used.[29]

After this procedure, the 3D measurement of the specimen points is straightforward: referring again to Fig. 1, for any object point P, the image plane coordinates ($c_P$, $r_P$) are measured and used in the system of Eqs. (6) and (7). Since both the camera and the laser plane parameters are known, the system can be solved for coordinates ($X_P$, $Y_P$, $Z_P$).

## C. Laser plane image analysis on ROI3

The angular measurement using the encoder is performed using the LP3 profiles illustrated in Fig. 3(f). For each position of the encoder, LP3 profiles of different lengths are acquired. Fig. 6 shows, as an example, four LP3 images at different

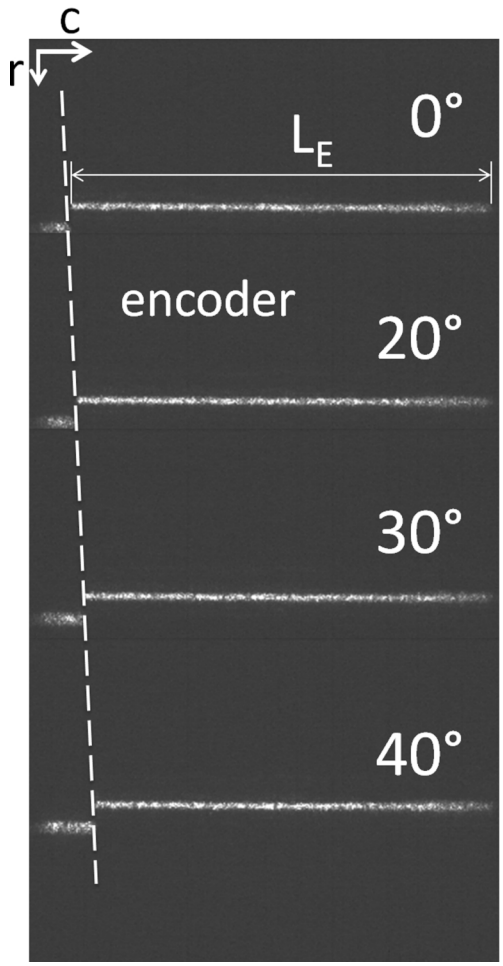


FIG. 6. Images of the line LP3 acquired at different angular positions.

rotation angles, demonstrating that their length $L_E$ linearly depends on the angular position of the encoder. Centers of gravity of LP3 are obtained again using Eq. (8), the corresponding vector $\{c_G, r_G\}$ is calculated, and $L_E$ is obtained as

$$L_E = \min\{c_G\}. \quad (9)$$

## V. SYSTEM SOFTWARE WORKFLOW

The duration of the cyclic contact tests can vary from 2 to 80 h. Wear and fatigue effects may occur within this time interval: the former yields small, progressive surface modifications, and the latter may occur abruptly without previous notice. Monitoring wear effects should be performed on a sampling basis, setting an adequate sampling frequency. The sampling interval, as well as the duration of each acquisition, should be user selectable. Monitoring fatigue effects, on the contrary, should start in correspondence to specific events, such as an abnormal vibration burst.[16] Here again, the duration of the acquisition should be user selectable. These requirements were easily satisfied using the triggered acquisition mode of the PROMON 501 camera, by selecting a pre-trigger value to acquire frames before and after the trigger event.

In the absence of a trigger, the three laser sources are set to "on" and the camera is set to "armed": it continuously grabs the images of the rotating specimen and records them into a circular buffer, of user selectable length, waiting for the trigger signal. When a trigger signal occurs, L2 is set to "off," and the camera grabs the images within the pre- and post-triggering time intervals. Then L1 is set to "off," while L2 is set to "on," and the camera grabs additional images. All the images are stored in the corresponding video files. A dedicated software has been developed to elaborate the video sequences as soon as they are available, following a producer-consumer architecture.

## VI. SYSTEM CHARACTERIZATION

### A. Calibration and performance of 3D measurements

The ability of the system to perform 3D measurements was tested using a master disk with the same nominal dimensions as the ones of the tested specimens (thickness 15 mm and diameter 60 mm), machine-worked to obtain a set of consecutive concentric rings (Fig. 7(a)). Each ring has a diameter which is nominally 0.50 mm smaller than the previous one: the result is a step-wise profile with a step depth h of nominally 0.25 mm along the Z axis. The frames acquired by the camera at 500 rpm underwent the 3D elaboration procedures illustrated in Section IV B. Fig. 7(b) shows the centers of gravity $(c_G, r_G)_n$ of LP2.

Fig. 8 shows the measured profile of the master disk vs the image columns. The dots in the graph are the measured points of the disk, and its measured steps are clearly visible in the figure. Points belonging to the same step have been interpolated by a straight line y = k (continuous lines in the figure), parallel to the axis c, where k is a constant. The value of this latter (measured h) and the corresponding standard uncertainty have been calculated for each step, using a least square method: the standard uncertainty is, on average, 33 $\mu$m, while the obtained best value is equal to 18 $\mu$m. The same measurements have been performed through a centesimal caliper, and Fig. 8 also shows the compatibility between the two different types of measure, with 95% level of confidence. The uncertainty related to the caliper measurements is considered as B type, according to Ref. 34. In particular, looking at the figure, the caliper measurements with their 95% uncertainty are also presented (symbols filled with black). They always overlap the 95% confidence intervals of the measurements obtained through the vision system.

### B. Encoder calibration and performance

Known angular displacements equal to 1° have been imposed using a motor rotary stage, with a positioning accuracy of 0.075° (≈0.0013 rad). At each position, the encoder


FIG. 7. (a) Master specimen for 3D stripe calibration; (b) $\{(c_G, r_G)\}$ plot of the centres of gravity of LP2.

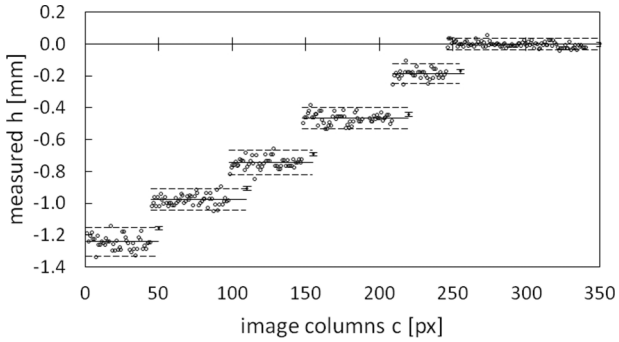


FIG. 8. 3D profile of the master specimen. The compatibility of the measurement is at a 95% level of confidence.

length $L_E$ has been measured, using the processing described in Section IV C. The calibration plot of Fig. 9 has been obtained. The resulting static sensitivity is equal to (3242.1 ± 4.8) $\times 10^{-5}$ rad/px, with a correlation coefficient r = 0.9996, demonstrating a good measurement linearity. The standard deviation $\sigma_0$ of the model results to be 0.050 rad (≈2.9°): since at $f_s$ = 500 rpm the angular variation between two subsequent frames is equal to $2\pi \times f_s/f_c$ = 0.14 rad (≈8.0°), the above value is more than adequate for our measurement purposes. The plot in Fig. 9 also shows the 95% prediction band and the model equation, which correlates the measured encoder length, in pixels, to the respective angular position.

## VII. EXPERIMENTAL RESULTS

### A. 2D surface analysis on end-of-test specimens

Fig. 10 shows typical examples of new (a) and end-of-cycle ((b) and (c)) specimens of rail. The new specimen of Fig. 10(a) is made of UIC 900 A, and the tested specimen of Fig. 10(b), equally of UIC 900 A, has rolled against a specimen made of Superlos®. The specimen of Fig. 10(c) is the same shown in Fig. 3 to illustrate the illumination source geometry, and is an end-of-life, rail specimen made of UIC 900 A, which rolled against ER8 with an emulsion of water and oil as a lubricant.

The new specimen appears, upon ambient light illumination, glossy and uniform, but at a deeper insight is characterized by evident milling grooves parallel to the circumference. The dry, end-of-test specimen exhibits a uniform roughness without traces of milling grooves, and this is direct evidence

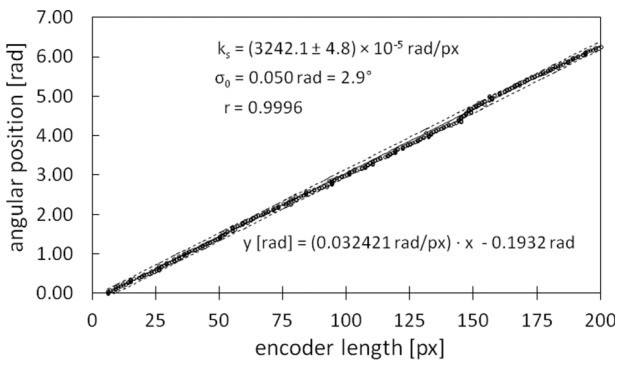


FIG. 9. Static calibration of the encoder.

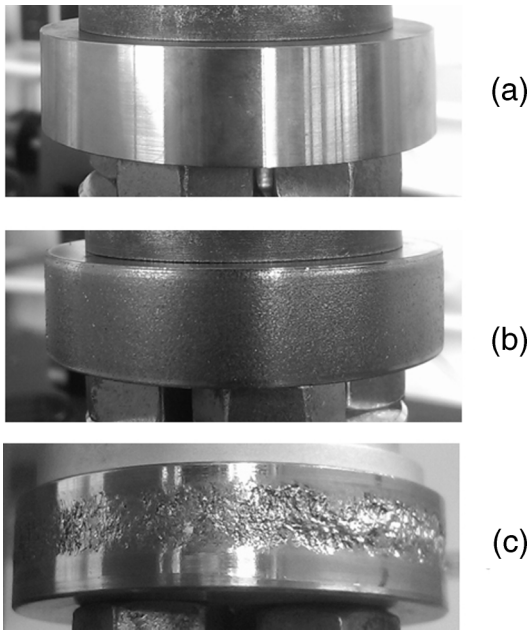


FIG. 10. Images of a rail specimen monitored during a dry RFC test. The specimen is made of UIC 900 A. (a) The specimen at 0 kcycles (new); (b) the same sample after 800 kcycles and after rolling against a specimen made of Superlos; (c) the sample after 800 kcycles and after rolling against a specimen made of ER8.

that wear has been the leading effect during tests.[16] The wet end-of-cycle specimen, on the other side, exhibits a markedly non-uniform damage aspect, characterized by deep, localized grooves as well as by still glossy regions.

The above qualitative appearance of the specimens has been quantitatively measured by means of our apparatus on a number of rail end-of-life specimens, both dry and wet. Here we used diffuse illumination LD with the image analysis procedures described in Section IV A. Fig. 11 shows a plot of the average damage ratio $R_B$, introduced in Eq. (4), as a function of the average blob area $A_B$, for all the tested specimens. In particular, in Fig. 11, the sample named "new" represents a new specimen; samples named LubA and LubB represent specimens which underwent a wet RCF test, against a wheel made of ER8 and a wheel made of Superlos®, respectively.

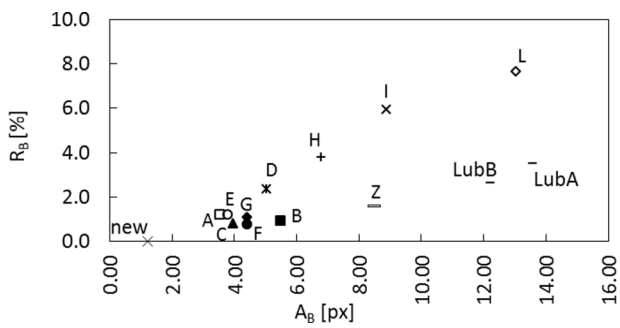


FIG. 11. Average damage ratio $R_B$ against average blob area $A_B$, for different rail specimens made of UIC 900 A, after 800 kcycles. A, C, G, and H rolled against wheels made of ER8. D, E, and I rolled against wheels made of Superlos. F and L rolled against wheels made of CL B. B rolled against a wheel made of CL C. LubA rolled against a specimen made of ER8 and LubB against one made of Superlos.

TABLE I. Classification of blobs.

| Class | Type | Area range (px) |
|---|---|---|
| C1 | Very small | 2–5 |
| C2 | Small | 6–15 |
| C3 | Regular | 16–30 |
| C4 | Large | 31–70 |
| C5 | Very large | >70 |

Samples from A to L represent specimens which underwent a dry test and differ one another for the type of steel of the counter-rolling wheel.

In all the experiments performed, the blobs have been classified according to their areas in px, as shown in Table I, that lists the area ranges defined as (i) very small, (ii) small, (iii) regular, (iv) large, and (v) very large. This classification will be particularly useful in the in-test analysis. In addition, the average blob area $A_B$ of each sample has been calculated.

Fig. 11 shows that the new specimen has a very small blob area $A_B$ (in the range of 1.2 px) and a negligible damage ratio $R_B$. This is quite consistent with the glossy appearance of the specimen. The dry-tested specimens exhibit average blob areas in the range 3.5–13 px and damage ratios in the range of 0.8%–7.7%. These ranges are quite large, in accordance with the findings published in Ref. 18, where rolling contact fatigue test have been performed to study how fatigue and wear proceed and interact. The results confirm that wear is the leading phenomenon, which removes layers of material from the surface and consequently affect the evolution of ratcheting. It results that specimens of similar materials after the same number of cycles can present different damage ratios depending on the interaction between RCF and wear. In addition, Fig. 11 shows that specimens with larger average values of $A_B$ also exhibit larger average damage ratios $R_B$ (see for instance specimens H, I, and L). These findings will be further supported by the evidence, from in-test acquisitions from a dry sample, that large and very large blobs are responsible of the large $R_B$ value.

The situation of the two lubricated specimens LubA and LubB is different: they are characterized by a large average area $A_B$, 12 px–14 px, but a small-medium damage ratio $R_B$ (about 3%). This is by no means surprising from a purely visual analysis of the specimen: in fact, as previously mentioned, its surface is characterized by craters and crests, only in correspondence to parts of their section, and this explains the large average blob areas. In the other parts of the specimen section, the material has still a glossy appearance, and this justifies the absence of very small blobs and the small $R_B$ value.

### B. In-test 2D analysis

As a verification of the potential of our apparatus to measure in-test damage evaluation of specimens, we performed 2D analysis during the test, to monitor the temporal evolution. Typical pictures of the diffused light-related ROI1 are assembled in Fig. 12. They refer to a wheel specimen before the test, and after 10, 20, 30, 50, 70, 100, and 130 kcycles (left top to bottom right). At each step, a 2 s video has been acquired and the analysis described in Section IV A has been carried out. The grey levels are, in the figure, inverted, to enhance the visibility of the blobs.

A clear change in the number, distribution, orientation, shape, and dimension of the blob is evident. The new sample (0k) is characterized by the virtual absence of blobs, with the exception of the lower section of the ROI, where tiny, almost horizontally periodical, vertically oriented blobs are evident as a consequence of the reflections from the milling grooves of the specimen. At 10 kcycles the number of blobs increases consistently, with a prevalence of the tiny, vertically oriented blobs, but with the appearance of blobs of larger dimensions, equally vertically oriented, generated by the connection of several tiny blobs. The overall damage area, corresponding to the total blob area, expands with reference to the overall ROI area, although an asymmetry in the appearance of the damaged area with respect to the ROI length is evident.

From 10 to 30 kcycles, the increase in blob number and dimension is mostly due to an expansion of the damaged area throughout the ROI length: the blobs are still mostly vertically

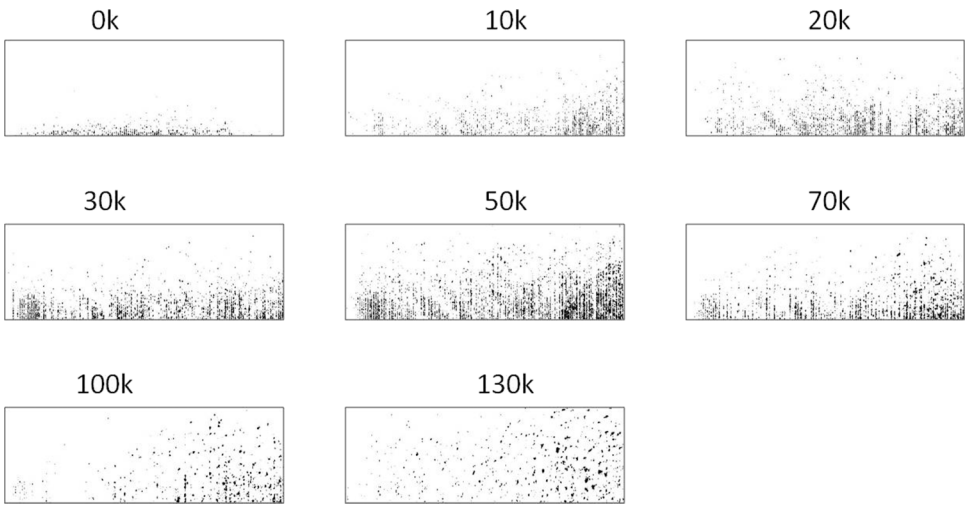


FIG. 12. Particles detected on frames acquired at different number of cycles, from the new specimen (0k) to the same specimen tested for 130 kcycles (130k). Grey levels of the images have been inverted to enhance the visibility of the blobs.

oriented, and a further aggregation of the tiny blobs into larger blobs is observed. At 50 kcycles the overall number of blobs is markedly increased, with a substantial increase in the number of larger blobs especially in the region where the former blob cluster was generated. From 50 to 70 kcycles the process seems to be stationary, although there is evidence of a decrease in the blob anisotropy (see for instance the blobs in the upper right side of the ROI). Finally, from 100 kcycles to the end of the test, the overall blob area decreases, with large blobs prevailing in area with respect to smaller blobs, and with both the former and the latter becoming almost circular.

It is worth noting that while the blob distribution in the specimen when it is new, or after 50 kcycles, remains quite constant along the circumference of the disk, between 20 and 30 kcycles it varies appreciably from one image to the other, highlighting instability in the wear process at the early stages of the test. To compensate for this distribution variation, the quantitative data described below have been obtained by averaging the ROI1 data over the entire circumference of the specimen.

Fig. 13 shows a plot of the average number of blobs of all the classes as a function of the number of cycles. For the ease of visualization, the figure has been split in two: Fig. 13(a) shows classes C1 and C2 (the most numerous), together with the total number of blobs (sum of C1…C5). Fig. 13(b) shows, on an expanded scale, the number of blobs of classes C3…C5. The discussion that follows refers to both figures at the same time. The first evidence is that, at 0 kcycles, the total number of blobs is very small, with prevalence of C1 blobs. Large and very large blobs are virtually absent. At 10 kcycles the overall number of blobs has already increased by a factor 4: there is still a marked prevalence of C1 and C2 blobs, although C3 blobs are present: C4 and C5 blobs are still very few.

At 20 kcycles the situation reverses: the total number of blobs, as well as the number of the blobs of all classes, slightly decreases. In particular, one can note the disappearance of very large blobs (C5). At 30 kcycles the number of blobs increases again, with all classes having the same behavior. This, at first sight, unexpected behavior finds its verification in the literature, where the samples were off-line analyzed with other methods (e.g., Barkhausen noise), and where the oscillating behavior was explained by a postulated initial instability of the wear process.[18]

At 50 kcycles the number of blobs reaches its maximum (which is clearly visible in Fig. 12). Classes C1, C2, and C3 also reach their maximum, whereas classes C4 and C5 still increase, up to 70 kcycles where they find their maximum, and classes C1, C2, C3, and the total slightly decrease. This situation can be defined the *plateau* of the process. At 100 and 130 kcycles the number of very small blobs drops consistently and remains stable, whereas all the other blobs, after the drop-down, tend to slightly increase.

An insight into the respective contribution of the blobs of all classes to the specimen damage is shown in Fig. 14, where the damage ratio $r_{B,i}$ defined by Eq. (4) is plotted. Again, in the new specimen, the damage is virtually absent: however, already at 10 kcycles the damage increases (by a factor 7) and the contribution to the damage is dominated by the very large blobs (C5), followed by the large blobs (C4).

Again at 20 kcycles the damage, still dominated by C5 blobs, decreases, and increases again at 30 kcycles, reaches its maximum at 50 kcycles, and then drops down again. This interesting result supports the fact that wear and RCF are concurrent phenomena; in particular, wear has a role in stabilizing the strain field for a high number of cycles, and prevents long crack formation.[18]

Finally, the asymmetry of the blobs (from Eq. (5)) at all stages of the test has been evaluated and shown in Fig. 15. In the new sample (0 kcycles), where they prevail in number, very small blobs have an H/W ratio slightly larger than 2. Blobs belonging to all the other classes have larger H/W values (up to 4 for C4 blobs), except for blobs of class C5 exhibiting smaller H/W values (however, these are very few). After 10 kcycles, the H/W ratio of blobs of all classes (except again from C5) decreases: C5 blob starts increasing. This can be explained

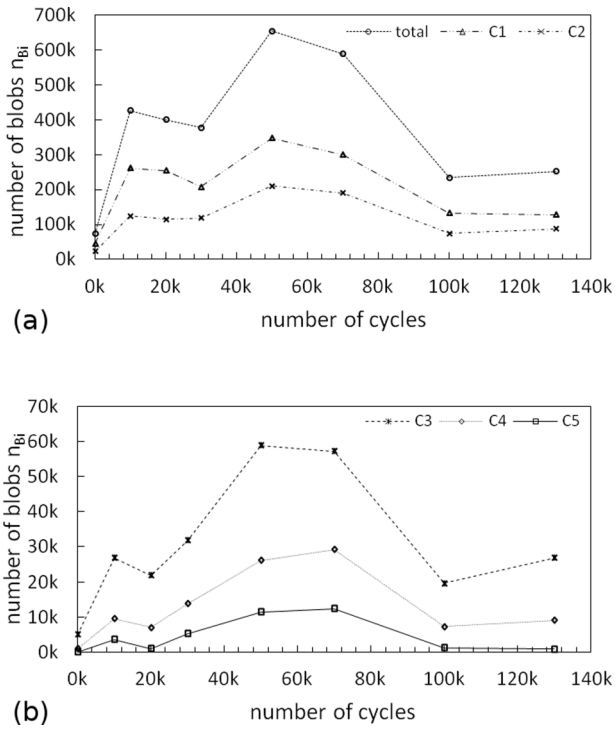


FIG. 13. Plot of the particle number $n_{B,i}$ as a function of the number of cycles. (a): total, C1 and C2 classes; (b) C3, C4, and C5 classes (expanded scale).

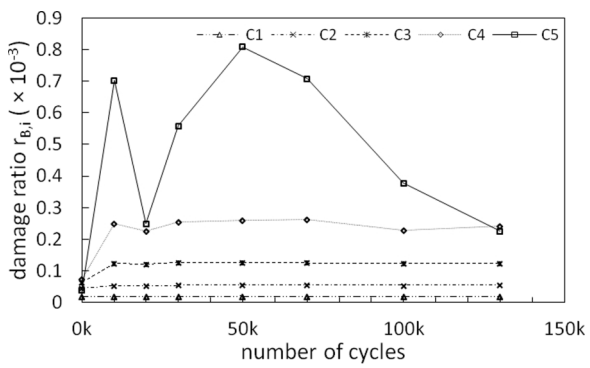


FIG. 14. Plot of the damage ratio $r_{B,i}$ vs. the number of cycles.

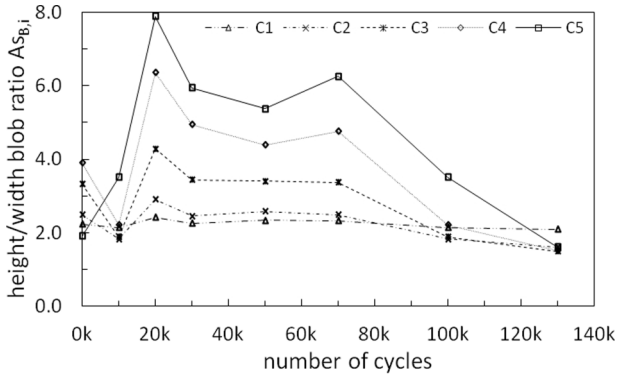


FIG. 15. Plot of the $As_{B,i}$ asymmetry index as a function of the number of cycles.

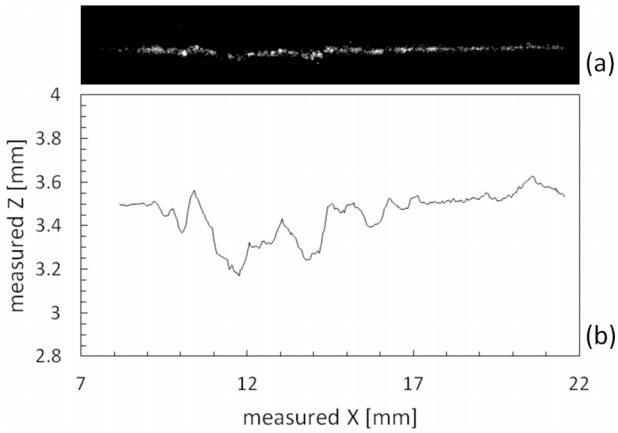


FIG. 16. Example of a 3D measurement on a rail specimen made of UIC 900 A, which has rolled 800 kcycles in a wet test against a wheel specimen made of ER8. (a) Acquired, after-threshold profile. (b) Measured profile.

by considering, as described earlier, the prevalence of small blobs: these are still oriented in the direction of the initial milling grooves, but since the milling grooves start flattening out, all blobs tend to decrease in asymmetry.

At 20 kcycles, smaller blobs still exhibit the same asymmetry, whereas larger blobs (C3 to C5) markedly increase in asymmetry (up to 8 for C5 blobs). This is evident from Fig. 12, from the degree of aggregation of the blobs in the vertical direction as they tend to increase in dimensions. At 30 kcycles the asymmetry of blobs of all classes decrease, and the decrease proceeds until 50 kcycles. At 70 kcycles the asymmetry of the larger C4 and C5 blobs reaches a second maximum (although lower than the previous one), whereas the smaller C2…C3 blobs start becoming more symmetric. Finally, after 70 kcycles, blobs of all classes decrease their asymmetry until values close to one (circular blobs), which is consistent with their appearance in Fig. 12 at 100 and 130 kcycles.

All the above description of the parameters derived by the 2D blob analysis is, in our opinion, a demonstration that the 2D analysis performed from the measurements with our apparatus during in-test fatigue tests are in good agreement with the visual evidence of the specimens, and of the scattered light from the pictures of Fig. 10, which are typical of a new and dry-tested specimen, regardless of being a rail or a wheel specimen. Still a doubt can be cast about the consistency of the dynamic behavior of the specimens during in-test measurements, with the parameters that could have been derived, had it been processed for a number of cycles reaching 800 000. From the literature,[18] there is evidence that after 130 kcycles the process becomes a periodic sequence of increased damage and subsequent flattening, resulting in the decrease in wheel diameter or rail height. This sequence may have a different ending, as shown in Fig. 11. The demonstration that the situation of the specimen after 130 kcycles is consistent with the situation after 800 kcycles is in the position, back in Fig. 11 of the non-previously described point Z, which is exactly the 130 kcycles specimen.

### C. 3D measurements

3D measurements of the specimen surfaces, following the procedure described in Section IV B, have been performed on several rail and wheel specimens. From the videos of the rotating specimens, the section with the 3D line profile LP2 on has been elaborated at a suitable number of angular positions, measured by means of the encoder Line Profile (LP3), to obtain the 3D profile over the section. As an example, in the following figures the case of the end of test rail specimen of UIC 900 A, following the wet test against the specimen made of ER8 (see Fig. 10(c)), is shown. Fig. 16(a), in particular, shows an example of a single profile as acquired by the camera, after thresholding. The profile has a considerably irregular appearance, due to the presence of craters, with some occasional discontinuities due to specular reflections from glossy high slope surface parts, due to detachments through fatigue phenomena. Fig 16(b) shows the corresponding z vs. x profile.

Finally, a planar view of the 3D profile of the specimen surface is shown in Fig. 17, assembled by combining the 3D profiles corresponding to 18 positions of the disk (i.e., every

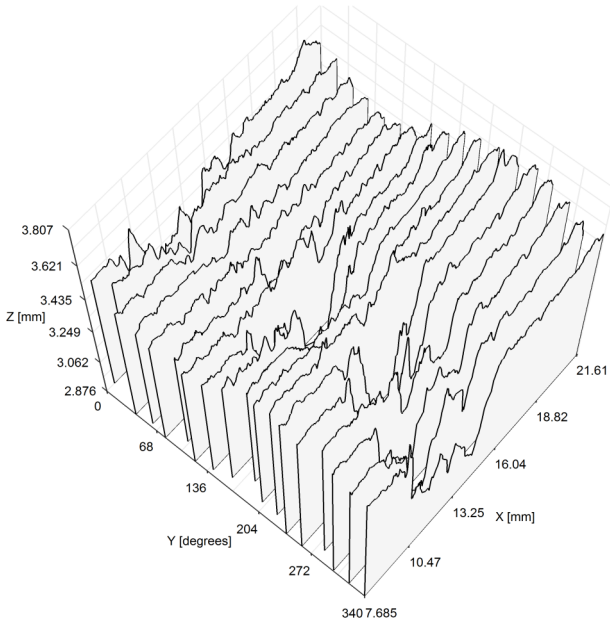


FIG. 17. 3D measurement of a specimen made of UIC 900 A, which has rolled 800 kcycles in a wet test against a wheel specimen made of ER8.

20°), as a function of the encoder angle. The analysis of the two figures, together with the results of the 3D calibration of Sec. VI A, demonstrates that the system is able to perform, even at high rotation speeds, very high-resolution measurements of the specimen surfaces.

## VIII. CONCLUSIONS

In this paper, the prototype of an optical system for high-speed image acquisition of rotating specimens on a twin-set test bench has been presented. The system combines, in a single assembly, (i) a fast triggerable video camera, (ii) a diffused semiconductor laser source for surface extended illumination, (iii) a 3D laser stripe for the acquisition of depth profiles based on optical triangulation, and (iv) a coaxial laser stripe for measuring the specimen angular position. Micro- and macro-topological measurements, as well as angular position measurements, can be effectively combined to the high-speed frame acquisition when the diffused laser beam and laser stripes are used as the illumination source for the specimen during the test, replacing incoherent light sources. The high laser brilliance makes these sources ideal also in the case of very short (tens of microseconds) exposure times.

The proposed prototype can be easily installed on the test bench and, just as easily, be mounted on an optical table when calibration is needed. It is adaptable to different types of tests, as the different laser sources offer complementary information about the surface of the specimens. Calibration of the system is simple and straightforward. The system is now installed in the test bench of a companion laboratory of our same department for rolling contact fatigue tests, without and with water/oil lubricants, and is yielding new information on the different types of damages, such as wear and fatigue, and on the behavior of different materials during the whole lifetime of the specimens.

## ACKNOWLEDGMENTS

We acknowledge the invaluable assistance of Professor A. Mazzù, Ing. M. Faccoli, and Ing. C. Petrogalli in the preparation of the specimens, and in the design of the experiments. We are also very grateful to Lucchini RS—Italy, which provided material and technical support, and we wish to thank Mr. Gabriele Coffetti, Mr. Silvio Bonometti, and Ing. Bruno Tratta for their support in the experimental activities.

[1]D. F. Cannon, K.-O. Edel, S. L. Grassie, and K. Sawley, Fatigue Fract. Eng. Mater. Struct. **26**, 865 (2003).
[2]U. Zerbst and S. Beretta, Eng. Failure Anal. **18**, 534 (2011).
[3]M. Ph. Papaelias, C. Roberts, and C. L. Davis, Proc. Inst. Mech. Eng., Part F **222**, 367 (2008).
[4]Z. Liu, W. Li, F. Xue, J. Xiafang, B. Bu, and Z. Yi, IEEE Trans. Magn. **51**, 1 (2015).
[5]Z. Li, M. Molodova, A. Núñez, and R. Dollevoet, IEEE Trans. Ind. Electron. **62**, 4385 (2015).
[6]Z. Liu, F. Li, B. Huang, and G. Zhang, J. Opt. Soc. Am. A **31**, 1721 (2014).
[7]Q. Li and S. Ren, IEEE Trans. Instrum. Meas. **61**, 2189 (2012).
[8]L. Jie, L. Siwei, L. Qingyong, Z. Hanqing, and R. Shengwei, in *IEEE International Symposium on Industrial Electronics (ISIE 2009)*, *Seoul, South Korea*, *5–8 July 2009* (IEEE, 2009), pp. 769–774.
[9]R. Stock and R. Pippan, Wear **314**, 44 (2014).
[10]N. Bosso and N. Zampieri, Shock Vib. **2014**, 1.
[11]U. Olofsson and T. Telliskivi, Wear **254**, 80 (2003).
[12]G. Zhou, C. He, G. Wen, and Q. Liu, Tribol. Int. **91**, 160 (2015).
[13]C. Kammerhofer, A. Hohenwarter, and R. Pippan, Wear **316**, 101 (2014).
[14]D. I. Fletcher and S. Lewis, Wear **298**, 57 (2013).
[15]T. Makino, T. Kato, and K. Hirakawa, Int. J. Fatigue **36**, 68 (2012).
[16]M. Lancini, I. Bodini, D. Vetturi, S. Pasinetti, A. Mazzù, L. Solazzi, C. Petrogalli, and M. Faccoli, ACTA IMEKO **4**, 66 (2015).
[17]A. Mazzù, L. Solazzi, M. Lancini, C. Petrogalli, A. Ghidini, and M. Faccoli, Wear **342-343**, 22 (2015).
[18]G. Donzella, M. Faccoli, A. Mazzù, C. Petrogalli, and R. Roberti, Wear **271**, 408 (2011).
[19]J. Sukuraman, S. Soleimani, P. De Baets, V. Rodriguez, K. Douterloigne, W. Philips, and M. Ando, Wear **296**, 702 (2012).
[20]G. Sansoni, M. Trebeschi, and F. Docchio, Sensors **9**, 568 (2009).
[21]G. Sansoni, P. Bellandi, and F. Docchio, Meas. Sci. Technol. **22**, 075302 (2011).
[22]W. Huang and R. Kovacevic, Int. J. Adv. Manuf. Technol. **63**, 235 (2012).
[23]R. Usamentiaga, J. Molleda, and D. F. Garcia, Mach. Vision Appl. **23**, 179 (2012).
[24]E. Kayahan, H. Oktem, F. Hacizade, H. Nasibov, and O. Gunogdu, Tribol. Int. **43**, 307 (2010).
[25]Y.-K. Fuh, K. C. Hsu, and J. R. Fan, Opt. Laser Eng. **50**, 312 (2012).
[26]G. A. Al-Kindi and B. Shirinzadeh, Int. J. Mach. Tools Manuf. **47**, 697 (2007).
[27]J. Zhang, M. Korsten, and P. Regtien, in *Proceedings of XVII IMEKO World Congress*, *Dubrovnik, Croatia*, *22–27 June 2003* (International Measurement Confederation, 2003), pp. 1960–1964.
[28]Datasheet PROMON 501 available at http://www.aostechnologies.com/.
[29]P. West, "A roadmap for building a machine vision system," available at http://www.imagenation.com/, 2005.
[30]T. B. Moeslund, *Introduction to Video and Image Processing—Building Real Systems and Applications*, Undergraduate Topics in Computer Science (Springer Verlag, London, 2012), p. 103.
[31]O. Faugeras, *Three-Dimensional Computer Vision—A Geometric Point of Viewpoint* (The MIT Press, Cambridge, MA, 1993), p. 7.
[32]J. Heikkillä and O. Silvén, in *Proceedings of IEEE Computer Society Conference on Computer Vision and Pattern Recognition, San Juan, PR, USA, 17–19 June 1997* (IEEE, 1997), pp. 1106–1112.
[33]Z. Zhang, IEEE Trans. Pattern Anal. Mach. Intell. **22**, 1330 (2000).
[34]JCGM 100:2008 "Evaluation of measurement data—Guide to the expression of uncertainty in measurement," 2008.